Symmetric Positive Semi-Definite FDTD Subgridding Algorithms in Both Space and Time for Accurate Analysis of Inhomogeneous Problems

Kaiyuan Zeng, *Student Member, IEEE*, and Dan Jiao, *Fellow, IEEE*

***Abstract*— In this article, we develop a systematic approach to derive symmetric positive semi-definite (SPD) finite-difference time-domain (FDTD) subgridding operators in both space and time for analyzing general inhomogeneous problems in an accurate fashion. The operators are SPD by construction and independent of the grid ratio. The resultant explicit time marching is guaranteed to be stable because such subgridding operators have only nonnegative real eigenvalues. Furthermore, the use of a time step local to the base grid and the subgrid is permitted without sacrificing stability and accuracy. Moreover, the algorithm takes the subgrid information into account to accurately analyze inhomogeneous problems. In addition, we provide an interpretation of the proposed subgridding operators and show how to implement them in the original difference equation-based FDTD framework. Extensive numerical experiments involving both 2- and 3-D subgrids with various grid ratios and inhomogeneities have demonstrated the stability, accuracy, and efficiency of the proposed new SPD subgridding algorithms.**

***Index Terms*— Finite-difference time-domain (FDTD) method, positive definite, positive semi-definite, spatial subgridding, stability, subgridding, subgridding in space and time, symmetric, temporal subgridding.**

I. Introduction

COMPARED with the conventional finite-difference time-domain (FDTD) method [1], [2], FDTD subgridding is an effective method to locally refine a grid for solving multiscale problems. Ideally, when simulating a multiscale problem, a subgridding method in both space and time not only reduces the number of unknowns but also permits the use of a local time step. In other words, the time step in a base grid is not restricted by the time step in the subgrid for a stable explicit time marching. Each grid can be simulated stably using its own time step and hence greatly accelerating an FDTD simulation. In literature, extensive work has been done to tackle the FDTD subgridding problem. In [3], a variable step size method (VSSM) was developed, providing a direct interpolation scheme to update fields in both base grid and subgrid. A mesh refinement algorithm (MRA) was presented in [4], requiring less computational memory and time. It has been observed that the stability and accuracy have always been two competing factors in developing FDTD subgridding algorithms. Accurate interpolations can always be done to obtain the field unknowns at the interface between a base grid and a subgrid. However, instability has been observed in the resulting time-domain simulation. Various methods have been proposed to fix the instability issue [5]–[8]. In [9]–[11], enforcing reciprocity of the fields has been proposed to ensure stability but accuracy is compromised. In [12], the subgrid was arranged in a special way in order to ensure the resultant numerical system to be symmetric.

To preserve accuracy, the existing subgridding schemes generally result in an unsymmetrical numerical system for arbitrary subgrid settings, where the curl of electric field and that of magnetic field do not transpose each other. The stability of the resultant time-domain simulation cannot be guaranteed using conventional explicit schemes. This is because an unsymmetrical matrix can support complex-valued and even negative eigenvalues, which would make a traditional explicit time marching absolutely unstable, a proof of which can be found in [13] and [14]. Recently, in [14], an accurate unsymmetrical FDTD subgridding method is developed to break this barrier. A new time marching scheme different from the traditional explicit time marching is developed to guarantee stability. However, this scheme requires the computation of a series expansion. Although the number of terms is small in the series, it increases the computational cost in time marching. Furthermore, the subgridding is only achieved in space, not in time.

Symmetric positive semi-definite (SPD) subgridding algorithms have also been developed to address the stability problem. In [15], a systematic approach is developed to make an FDTD subgridding algorithm SPD regardless of the grid ratio and the grid arrangement. As a result, only nonnegative real eigenvalues exist, and the resultant time marching is ensured to be stable. In [15], a 3-D subgridding operator is demonstrated with a capability of local time stepping. However, the solution of the base grid unknowns is decoupled from that of the subgrid to make the resulting system matrix SPD. Such a scheme suffers from inaccuracy when subgrid regions involve strong inhomogeneity. The 2-D subgridding operator in [15] can handle inhomogeneous problems accurately, however, it is

Manuscript received April 23, 2019; revised October 7, 2019; accepted November 19, 2019. Date of publication January 14, 2020; date of current version April 7, 2020. This work was supported in part by the NSF under Award 1619062 and in part by the Defense Advanced Research Projects Agency under Award FA8650-18-2-7847. *(Corresponding author: Dan Jiao.)*

The authors are with the School of Electrical and Computer Engineering, Purdue University, West Lafayette, IN 47907 USA (e-mail: djiao@purdue.edu).

Color versions of one or more of the figures in this article are available online at http://ieeexplore.ieee.org.

Digital Object Identifier 10.1109/TAP.2020.2964943

only achieved in space, not in time. As a result, a local time stepping is not permitted, and the time step in the base grid is restricted by that in the subgrid, and vice versa.

In this article, we propose a systematic approach to develop SPD FDTD subgridding operators in both space and time regardless of the grid settings, and accurate for analyzing both 2- and 3-D inhomogeneous problems. This approach and resultant 2- and 3-D subgridding operators successfully remove the problems encountered in the existing SPD FDTD algorithms. The subgridding is achieved in both space and time, and meanwhile it is accurate for solving inhomogeneous problems. We also provide an explanation of the proposed operators in the original difference equation-based FDTD and show how to implement them in the original FDTD without using matrix operators. This explanation provides many new findings on the development of FDTD subgridding schemes, which are difficult to conceive in the traditional FDTD. For example, in the proposed temporal subgridding algorithm, the electric field at the interface between the base grid and the subgrid is split into two components. One is generated from a partial curl of **H** operation using the *H*-fields in the base grid with a base-grid time step for time marching. The other is generated from the remaining curl of **H** operation using the *H*-fields in the subgrid with a subgrid time step. The two are then added to obtain the total interface field before proceeding to the next time step. Extensive numerical experiments and comparisons with the state-of-the-art subgridding algorithms like [14] and [15] have been carried out. The new algorithms are shown to outperform existing work, and its accuracy, efficiency, and stability are demonstrated.

This article is organized as follows. In Section II, we briefly review the background of this article, including a patch-based single-grid FDTD formulation which facilitates an algebraic derivation of subgridding operators, and the stability analysis of an FDTD time marching scheme. In Section III, we develop a systematic approach to develop SPD FDTD subgridding operators in both space and time. In Section IV, we present the details of the proposed 2-D SPD subgridding operator, with accuracy taken into consideration. In Section V, we elaborate on the 3-D SPD subgridding algorithms. In Section VI, numerous examples are provided to demonstrate the performance of the proposed algorithms. In Section VII, we draw our conclusions.

II. Preliminaries

First, we provide a brief review of the patch-based single-grid FDTD formulation, which is developed in [17]. It is used in this article to facilitate the development of a generic SPD subgridding algorithm, as this formulation reveals clearly how the submatrices in different regions are assembled in an FDTD to build a global system matrix.

The formulation is valid for both 2- and 3-D grids. Let $\{e\}$ be a global electric field unknown vector of length N_e, and $\{h\}$ being a global magnetic field unknown vector of length N_h. The FDTD can be written into the following form:

$$\mathbf{S}_e\{e\} = -\mathbf{D}_\mu\{\dot{h}\} \tag{1}$$

$$\mathbf{S}_h\{h\} = \mathbf{D}_\epsilon\{\dot{e}\} + \mathbf{D}_\sigma\{e\} + \{j\} \tag{2}$$

where a dot above a letter denotes the first-order time derivative, $\{j\}$ represents a current source vector, and $\mathbf{D}_\mu$, $\mathbf{D}_\sigma$, and $\mathbf{D}_\epsilon$ are diagonal matrices of permeability, conductivity, and permittivity, respectively.

Based on the patch-based single-grid formulation, each row of $\mathbf{S}_e$ in (1) corresponds to one patch in the grid, and when multiplied by $\{e\}$, it produces the magnetic field located at the patch center and normal to the patch. Take the ith row of $\mathbf{S}_e$ as an example, it can be written as

$$\mathbf{S}_e^{(i)} = \left\{-\frac{1}{L_i}, \frac{1}{L_i}, \frac{1}{W_i}, -\frac{1}{W_i}\right\} \oplus zeros(1, N_e) \tag{3}$$

which has only four nonzero elements, and L_i and W_i are the two side lengths of the ith patch. A reference normal direction is defined for every patch, which is also **H**'s reference direction on the patch. Using the right-hand rule, with the right thumb pointing to the reference normal direction, if the electric field edge's direction is along the direction encircling the normal direction, then a plus sign is used; otherwise, a negative sign appears in (3). The $\oplus$ denotes an extended addition by adding the four nonzero elements upon a zero vector of length N_e, based on the global indexes of the four electric field unknowns on the patch. Similarly, for the ith patch, we generate a column vector

$$\mathbf{S}_h^{(i)} = \left\{-\frac{1}{L_i}, \frac{1}{L_i}, \frac{1}{W_i}, -\frac{1}{W_i}\right\}^T \oplus zeros(N_e, 1) \tag{4}$$

which is nothing but the transpose of (3), thus

$$\mathbf{S}_h = \mathbf{S}_e^T. \tag{5}$$

As can be seen, a column i of $\mathbf{S}_h$ has also at most four nonzero entries located at the rows corresponding to the four electric fields of patch i.

Eliminating $\{h\}$ from (1) and (2), we obtain

$$\mathbf{D}_\epsilon\{\ddot{e}\} + \mathbf{D}_\sigma\{\dot{e}\} + \mathbf{S}\{e\} = -\{\dot{j}\} \tag{6}$$

where $\mathbf{S}$ can be represented as

$$\mathbf{S} = \mathbf{S}_h\mathbf{D}_{\mu^{-1}}\mathbf{S}_e = \sum_{i=1}^{N_h} \mu_i^{-1}\left(\mathbf{S}_h^{(i)}\right)_{N_e\times 1}\left(\mathbf{S}_e^{(i)}\right)_{1\times N_e} \tag{7}$$

which is a sum of the rank-1 matrix $\mathbf{S}_h^{(i)}\mathbf{S}_e^{(i)}$ over all the patches.

A leap-frog-based time marching of (1) and (2) is equivalent to a central-difference-based explicit time marching of (6), which can be readily proved. The stability of the resulting explicit marching is guaranteed if the following condition is satisfied:

$$\Delta t \le \frac{2}{\sqrt{\lambda_{max}}} \tag{8}$$

where λ_{max} stands for the largest eigenvalue of $\mathbf{D}_\epsilon^{-1}\mathbf{S}$ [16]. In the conventional FDTD for a uniform grid, $\mathbf{S}$ is SPD as evident from (7) and (5). Since $\mathbf{D}_\epsilon$ is also a symmetric positive definite, the eigenvalues of $\mathbf{D}_\epsilon^{-1}\mathbf{S}$ are nonnegative real. As a result, a real-valued time step can always be found to satisfy (8). However, in an FDTD subgridding scheme, due to the mismatch between the base grid and the subgrid,

various unsymmetrical interpolations are used to obtain the unknown fields at the subgrid interface, making the resulting rank-1 matrix of each patch not symmetric. As a result, $\mathbf{S}$ is unsymmetrical in general, which involves complex or negative eigenvalues in nature. When such eigenvalues exist, a traditional explicit time marching is absolutely unstable, which has been proved in [13] and that is why many FDTD subgridding algorithms cannot ensure stability.

III. Systematic Approach for Developing SPD Subgridding Algorithms in Both Space and Time

In this section, we present a systematic approach for developing SPD FDTD subgridding algorithms in both space and time. This approach is also algebraic and suitable for general subgridding settings in both 2- and 3-D problems.

From (6) and (7), we can analyze how the equations in different domains are assembled in the FDTD to simulate the entire problem. Consider two domains, (6) can be rewritten as

$$\mathbf{D}_\epsilon\{\ddot{e}\} + \mathbf{D}_\sigma\{\dot{e}\} = -[\mathbf{S}_{h,1}\mathbf{D}_{\mu_1^{-1}}\mathbf{S}_{e,1} + \mathbf{S}_{h,2}\mathbf{D}_{\mu_2^{-1}}\mathbf{S}_{e,2}]\{e\} \quad (9)$$

where $\mathbf{S}_{h,1(2)}$ has all the column vectors generated from the patches in domain 1 (2), and $\mathbf{S}_{e,1(2)}$ comprises all the row vectors from the patches in domain 1 (2). Here the source term is omitted to focus on the assembling mechanism in the FDTD. As can been seen, the total $\mathbf{S}$ is an addition of each domain's $\mathbf{S}$, which is the same as the assembling procedure in a finite-element method (FEM). Each patch's $\mathbf{S}$ is assembled to obtain a global $\mathbf{S}$ based on the index of a global unknown vector. However, the $\mathbf{D}_\epsilon$ and $\mathbf{D}_\sigma$ are not added up from each domain's contribution. They are diagonal matrices, whose entries are the permittivity or conductivity at the corresponding e's location. Shall they be assembled from each patch's contribution like that in an FEM, then the diagonal entry would be a multiple of the permittivity or conductivity. This unique assembling procedure in the FDTD, originated from the use of a dual grid, also renders its SPD subgridding scheme more difficult to develop, as compared to the FEM in handling a nonconformal mesh.

Based on (9), we can express the electric filed unknown as the addition of two contributions: one is from domain 1, expressed by the first term of the right-hand side of (9); the other is from domain 2 represented by the second term. Hence, we can rewrite (9) as a two-row system

$$\mathbf{D}_\epsilon\{\ddot{e}\}_1 + \mathbf{D}_\sigma\{\dot{e}\}_1 = -\mathbf{S}_{h,1}\mathbf{D}_{\mu_1^{-1}}\mathbf{S}_{e,1}\{e\} \quad (10)$$

$$\mathbf{D}_\epsilon\{\ddot{e}\}_2 + \mathbf{D}_\sigma\{\dot{e}\}_2 = -\mathbf{S}_{h,2}\mathbf{D}_{\mu_2^{-1}}\mathbf{S}_{e,2}\{e\} \quad (11)$$

with

$$\{e\} = \{e\}_1 + \{e\}_2 \quad (12)$$

which stitches the two domains together. Neither $\{e\}_1$ nor $\{e\}_2$ provides a complete solution of $\{e\}$. This is because for an interface e unknown between domain 1 and domain 2, (10) yields the curl of $\mathbf{H}$ from domain 1 patches, and (11) generates the curl of $\mathbf{H}$ from domain 2 patches, and the addition shown in (12) is required to complete the whole curl of $\mathbf{H}$ operation to produce the electric field on the interface.

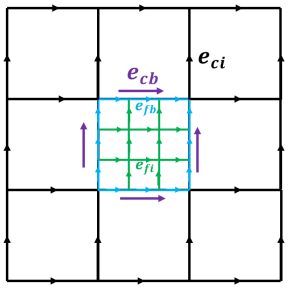

Fig. 1. Illustration of a subgrid embedded in a base grid and different kinds of unknowns.

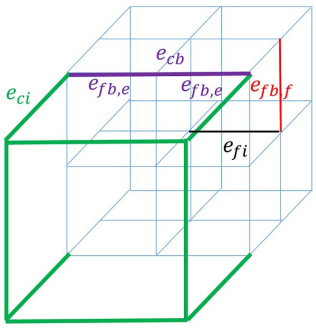

Fig. 2. Illustration of a subgrid embedded in a base grid in a 3-D grid.

If the two regions are a base grid and a subgrid, respectively, the same principle applies to add the equations from each region. In what follows, we denote the base-grid region by c, as a $c$oarse mesh is often used in the base grid; and the subgrid region by f, standing for a $f$iner mesh in the subgrid. As illustrated in Figs. 1 and 2, we use $\{e_{fb}\}$, $\{e_{fi}\}$, $\{e_{cb}\}$, and $\{e_{ci}\}$ to denote the electric field unknowns (edges) on the subgrid boundary, inside the subgrid, on the base grid boundary that overlaps with the subgrid boundary, and inside the base grid, respectively. Obviously, one $\{e_{cb}\}$ overlaps with multiple $\{e_{fb}\}$.

To maintain the field tangential continuity at the interface between the base grid and the subgrid, we should use only one set of $\mathbf{E}$ unknowns between $\{e_{cb}\}$ and $\{e_{fb}\}$. If we use $\{e_{cb}\}$ as the set, the global unknown $\mathbf{E}$ vector is composed of

$$\{e\}_{N_e\times 1} = \{e_{ci}, e_{fi}, e_{cb}\}^T \quad (13)$$

with a total number of $\mathbf{E}$ unknowns being

$$N_e = \#e_{ci} + \#e_{fi} + \#e_{cb}. \quad (14)$$

If we use $\{e_{fb}\}$, we have the following $\{e_{sub}\}$ being the global $\mathbf{E}$ vector:

$$\{e_{sub}\}_{N_{e,sub}\times 1} = \{e_{ci}, e_{fi}, e_{fb}\}^T \quad (15)$$

whose length is

$$N_{e,sub} = \#e_{ci} + \#e_{fi} + \#e_{fb}. \quad (16)$$

If the vector in (13) is used as a global unknown vector, the e's solution contributed from the base grid, defined as $\{e\}_p$, can be expressed as

$$\mathbf{D}_\epsilon\{\ddot{e}\}_p + \mathbf{D}_\sigma\{\dot{e}\}_p = -\mathbf{S}_{h,c}\mathbf{D}_{\mu_c^{-1}}\mathbf{S}_{e,c}\{e\} \quad (17)$$

where $\mathbf{S}_{e,c}$ is obtained from all of the patches in the base grid, and $\mathbf{S}_{h,c}$ is the transpose of $\mathbf{S}_{e,c}$. Similarly, the e's solution

contributed from the subgrid, defined as $\{e\}_m$, can be written into

$$\mathbf{D}_{\epsilon,sub}\{\ddot{e}_{sub}\}_m+\mathbf{D}_{\sigma,sub}\{\dot{e_{sub}}\}_m=-\mathbf{S}_{h,f}\mathbf{D}_{\mu_f^{-1}}\mathbf{S}_{e,f}\{e_{sub}\} \quad (18)$$

where $\mathbf{S}_{e,f}$ is obtained from all of the patches in the subgrid and $\mathbf{S}_{h,f}$ is its transpose.

To combine (17) and (18), we can represent $\{e_{sub}\}$ in terms of $\{e\}$. Since only the subgrid boundary unknowns need such a transformation, we can write

$$\{e_{fb}\}=\mathbf{P}_{fc}\{e_{cb}\} \quad (19)$$

where $\mathbf{P}_{fc}$ is used to interpolate $\{e_{fb}\}$ from $\{e_{cb}\}$. Subsequently, we can write

$$\{e_{sub}\}_{N_{e,sub}\times 1}=\mathbf{P}\{e\}_{N_e\times 1} \quad (20)$$

and $\mathbf{P}$, whose size is $N_{e,sub}\times N_e$, has the following form:

$$\mathbf{P}=\begin{bmatrix}(\mathbf{I})_{\#e_{ci}\times\#e_{ci}} & 0 & 0\\ 0 & (\mathbf{I})_{\#e_{fi}\times\#e_{fi}} & 0\\ 0 & 0 & (\mathbf{P}_{fc})_{\#e_{fb}\times\#e_{cb}}\end{bmatrix} \quad (21)$$

in which $\mathbf{I}$ denotes an identity matrix, and the subscripts denote matrix dimensions.

Using the above transformation, (18) can be rewritten as

$$\mathbf{D}_{\epsilon,sub}\mathbf{P}\{\ddot{e}\}_m+\mathbf{D}_{\sigma,sub}\mathbf{P}\{\dot{e}\}_m=-\mathbf{S}_{h,f}\mathbf{D}_{\mu_f^{-1}}\mathbf{S}_{e,f}\mathbf{P}\{e\}. \quad (22)$$

To obtain a symmetric system of equations, we multiply both sides of (22) by $\mathbf{P}^T$, obtaining

$$\mathbf{P}^T\mathbf{D}_{\epsilon,sub}\mathbf{P}\{\ddot{e}\}_m+\mathbf{P}^T\mathbf{D}_{\sigma,sub}\mathbf{P}\{\dot{e}\}_m=-\mathbf{P}^T\mathbf{S}_{h,f}\mathbf{D}_{\mu_f^{-1}}\mathbf{S}_{e,f}\mathbf{P}\{e\}. \quad (23)$$

Combining (17) and (23) with the following:

$$\{e\}=\{e\}_p+\{e\}_m \quad (24)$$

we obtain the global system of equations for solving e when subgrids are present.

In [15], the 2-D subgridding algorithm does not permit a local time stepping, i.e., allowing for the use of a time step in the base grid local to the base grid regardless of the subgrid. As a result, one has to use a smaller time step restricted by the finer space step in the subgrid for the time marching in the base grid. To permit a local time stepping, in this article, we propose to solve the following $\{e\}_p$ and $\{e\}_m$ systems of equations instead of $\{e\}$ directly:

$$\begin{bmatrix}\mathbf{D}_\epsilon & 0\\ 0 & \mathbf{P}^T\mathbf{D}_{\epsilon,sub}\mathbf{P}\end{bmatrix}\begin{bmatrix}\ddot{e}_p\\ \ddot{e}_m\end{bmatrix}+\begin{bmatrix}\mathbf{D}_\sigma & 0\\ 0 & \mathbf{P}^T\mathbf{D}_{\sigma,sub}\mathbf{P}\end{bmatrix}\begin{bmatrix}\dot{e}_p\\ \dot{e}_m\end{bmatrix}+\begin{bmatrix}\mathbf{S}_{cc} & \mathbf{S}_{cc}\\ \mathbf{P}^T\mathbf{S}_{ff}\mathbf{P} & \mathbf{P}^T\mathbf{S}_{ff}\mathbf{P}\end{bmatrix}\begin{bmatrix}e_p\\ e_m\end{bmatrix}=b \quad (25)$$

where

$$\begin{aligned}\mathbf{S}_{cc}&=\mathbf{S}_{h,c}\mathbf{D}_{\mu_c^{-1}}\mathbf{S}_{e,c}\\ \mathbf{S}_{ff}&=\mathbf{S}_{h,f}\mathbf{D}_{\mu_f^{-1}}\mathbf{S}_{e,f}.\end{aligned} \quad (26)$$

If the new system (25) can be stably simulated, we can prove the time step for simulating $\{e\}_p$ is determined by the base grid, instead of the subgrid, as the following. Rewriting (25) in frequency domain, we have

$$\begin{bmatrix}-\omega^2\mathbf{D}_\epsilon+\mathbf{S}_{cc} & \mathbf{S}_{cc}\\ \mathbf{P}^T\mathbf{S}_{ff}\mathbf{P} & -\omega^2\mathbf{D}_\epsilon+\mathbf{P}^T\mathbf{S}_{ff}\mathbf{P}\end{bmatrix}\begin{bmatrix}e_p\\ e_m\end{bmatrix}=b(\omega). \quad (27)$$

Eliminating $\{e\}_m$, the $\{e\}_p$ satisfies

$$[-\omega^2\mathbf{D}_\epsilon+\mathbf{S}_{cc}(\mathbf{I}-\mathbf{A}_{ff}^{-1}\mathbf{S}_{ff})]e_p=b \quad (28)$$

where $\mathbf{I}$ is an identity matrix and $\mathbf{A}_{ff}=-\omega^2\mathbf{D}_\epsilon+\mathbf{P}^T\mathbf{S}_{ff}\mathbf{P}$. The $\mathbf{S}$ part in (28) is $\mathbf{S}_{cc}$ right multiplied by another matrix, and hence the field solution e_p is still spanned in the space of $\mathbf{S}_{cc}$'s eigenvectors (from the base grid), which guarantees that the base grid time step is not restricted by the subgrid region. Similarly it can be proven that the subgrid can be simulated using the time step allowed for stably simulating the $\mathbf{S}_{ff}$ modes, thus local to the subgrid.

In our conference paper [18], we prove that the $\mathbf{S}$-related matrix in (25) is positive semi-definite. This is because the eigenvalues λ and the eigenvectors x of the $\mathbf{S}$-related matrix satisfy

$$\mathbf{S}_{new}x=\begin{bmatrix}\mathbf{S}_{cc} & \mathbf{S}_{cc}\\ \mathbf{P}^T\mathbf{S}_{ff}\mathbf{P} & \mathbf{P}^T\mathbf{S}_{ff}\mathbf{P}\end{bmatrix}\begin{Bmatrix}x1\\ x2\end{Bmatrix}=\lambda\begin{Bmatrix}x1\\ x2\end{Bmatrix} \quad (29)$$

hence, $\lambda(x1+x2)=(\mathbf{S}_{cc}+\mathbf{P}^T\mathbf{S}_{ff}\mathbf{P})(x1+x2)$. Since both $\mathbf{S}_{cc}$ and $\mathbf{P}^T\mathbf{S}_{ff}\mathbf{P}$ are SPD, the $\mathbf{S}_{new}$'s eigenvalues are also non-negative real. However, this proof does not lead to the proof that the $\mathbf{D}_{new}^{-1}\mathbf{S}_{new}$ also has nonnegative real eigenvalues, where $\mathbf{D}_{new}$ is the block diagonal matrix in front of the second-order time derivative of $\{e\}$ in (25). Since $\mathbf{S}_{new}$ is unsymmetrical now, even though it has nonnegative real eigenvalues, it does not guarantee that $\mathbf{D}_{new}^{-1}\mathbf{S}_{new}$ has only nonnegative real eigenvalues for arbitrary $\mathbf{P}$ and hence $\mathbf{D}_{new}$. Thus, the resulting explicit time marching would not be stable.

To systematically develop a subgridding algorithm which is SPD by construction, we carried out the following analysis. First, we should realize that since e_{fb} and e_{cb} overlap, they share the same material parameter, and hence

$$\mathbf{P}^T\mathbf{D}_{\epsilon,sub}\mathbf{P}=\mathbf{P}^T\mathbf{P}\mathbf{D}_\epsilon \quad (30)$$

$$\mathbf{P}^T\mathbf{D}_{\sigma,sub}\mathbf{P}=\mathbf{P}^T\mathbf{P}\mathbf{D}_\sigma. \quad (31)$$

As a result, (23) can be rewritten as

$$\mathbf{D}_\epsilon\{\ddot{e}\}_m+\mathbf{D}_\sigma\{\dot{e}\}_m=-(\mathbf{P}^T\mathbf{P})^{-1}\mathbf{P}^T\mathbf{S}_{h,f}\mathbf{D}_{\mu_f^{-1}}\mathbf{S}_{e,f}\mathbf{P}\{e\}. \quad (32)$$

Adding the above upon (17), the whole system of equations for solving $\{e\}$ can be written as

$$\mathbf{D}_\epsilon\{\ddot{e}\}+\mathbf{D}_\sigma\{\dot{e}\}=-[\mathbf{S}_{cc}+(\mathbf{P}^T\mathbf{P})^{-1}\mathbf{P}^T\mathbf{S}_{ff}\mathbf{P}]\{e\} \quad (33)$$

which can be written in short as

$$\mathbf{D}_\epsilon\{\ddot{e}\}+\mathbf{D}_\sigma\{\dot{e}\}=-\mathbf{S}_{total}\{e\} \quad (34)$$

where

$$\mathbf{S}_{total}=\mathbf{S}_{cc}+(\mathbf{P}^T\mathbf{P})^{-1}\mathbf{P}^T\mathbf{S}_{ff}\mathbf{P}. \quad (35)$$

The stability of (33), which is also that of (25), is governed by the property of $\mathbf{D}_\epsilon^{-1}\mathbf{S}_{total}$. Since $\mathbf{D}_\epsilon$ is symmetric and positive definite, the stability is governed by the property of $\mathbf{S}_{total}$. If $\mathbf{S}_{total}$ is symmetric and positive semi-definite,

then $\mathbf{D}_\epsilon$ and $\mathbf{S}_{total}$ form an SPD eigenvalue problem, whose eigenvalues are known to be nonnegative real. Unfortunately, the $\mathbf{S}_{total}$ shown in (35) is not symmetric for general $\mathbf{P}$. However, if $\mathbf{P}^{-1} = \mathbf{P}^T$, then obviously $\mathbf{S}_{total}$ would become symmetric. Since $\mathbf{P}$ is not a square matrix because the subgrid does not match the base grid, $\mathbf{P}^{-1}$ does not exist. Nevertheless, if we can make $\mathbf{P}^T\mathbf{P}$ an identity matrix, or an identity matrix scaled by a positive coefficient, then (35) is also symmetric and positive semi-definite. Let $\mathbf{P}^T\mathbf{P} = d\mathbf{I}$, we have

$$\mathbf{S}_{total} = \mathbf{S}_{cc} + d^{-1}\mathbf{P}^T\mathbf{S}_{ff}\mathbf{P} \tag{36}$$

which is symmetric and positive semi-definite.

The aforementioned provides a theoretical framework to develop an FDTD subgridding algorithm that is SPD by construction. The only thing left for consideration is accuracy, i.e., we have to make sure the field solution obtained from the resulting system is accurate. Based on the ideas presented in this section, we successfully develop 2- and 3-D SPD subgridding algorithms in both space and time, which are also accurate, the details of which are presented in Section IV.

IV. SPD 2-D Subgridding Algorithm in Space and Time

In this section, we first present an accurate 2-D SPD subgridding operator in space and time and then provide an interpretation of the operator in the original FDTD framework.

A. 2-D Subgridding Operator

For 2-D cases, let the grid ratio be n, then there are n subgrid boundary unknowns e_{fb} overlapping with the e_{cb} from the base grid, as illustrated in Fig. 1. We need to find a good choice of $\mathbf{P}$ that can result in a system matrix shown in (36). The $\mathbf{P}$ in [15] satisfies this requirement after certain modifications. Specifically, the following $\mathbf{P}_{fc}$ is employed:

$$\mathbf{P}_{fc} = [1 \quad 1 \quad 1 \quad \cdots \quad 1]^T_{n\times 1}. \tag{37}$$

For such a choice of $\mathbf{P}_{fc}$, $(\mathbf{P}^T\mathbf{P})^{-1}$ is a diagonal matrix of

$$(\mathbf{P}^T\mathbf{P})^{-1} = \begin{bmatrix} \mathbf{I}_{\#e_{ci}} & 0 & 0 \\ 0 & \mathbf{I}_{\#e_{fi}} & 0 \\ 0 & 0 & n^{-1}\mathbf{I}_{\#e_{cb}} \end{bmatrix} \tag{38}$$

where $\mathbf{I}$ denotes an identity matrix whose size is specified by the subscript and # denotes the cardinality of a set.

Although (38) is diagonal, it cannot be written as an identity matrix scaled by a constant. However, we can change the diagonal block corresponding to the e_{ci} from $\mathbf{I}$ to $n^{-1}\mathbf{I}$. This would not change (33) since the $\mathbf{S}_{ff}$ term is zero in the rows/columns corresponding to e_{ci}. In other words, $\mathbf{S}_{ff}$ does not involve unknowns in the base grid. We can also change the diagonal block corresponding to the e_{fi} from $\mathbf{I}$ to $n^{-1}\mathbf{I}$. This will change the $\mathbf{S}_{ff}$ term. However, we can scale the left-hand side matrices corresponding to the e_{fi} in the same way. As a result, the solution would not be changed. After the modifications, we obtain the following system of equations:

$$\mathbf{D}\mathbf{D}_\epsilon\{\ddot{e}\} + \mathbf{D}\mathbf{D}_\sigma\{\dot{e}\} = -[\mathbf{S}_{cc} + n^{-1}\mathbf{P}^T\mathbf{S}_{ff}\mathbf{P}]\{e\} \tag{39}$$

where $\mathbf{D} = diag\{\{1\}_{\#e_{ci}}, \{1/n\}_{\#e_{fi}}, \{1\}_{\#e_{cb}}\}$, a diagonal matrix made of the entries shown in the braces. The above system is clearly SPD, whose solution is also the same as (33), thus not changed.

Although (39) is SPD, we find it is not very accurate. This is because the cell size is different for the subgrid patches and the base grid patches. We need to use an average length to calculate the electric field of e_{cb} from the curl of $\mathbf{H}$. To see this point clearly, consider one e_{cb} unknown whose global index is i, its corresponding row of equation in (39) can be written as

$$\epsilon_i e_{cb,i} + \sigma_i e_{cb,i} = -\left[\frac{1}{L_c}\dot{h}_{base} - \frac{1}{nL_f}\sum_{j=1}^{n}\dot{h}_{s,j}\right] \tag{40}$$

in which ϵ_i and σ_i denote the permittivity and conductivity, respectively, at the point of $e_{cb,i}$, L_c denotes the base grid cell size, and L_f is the subgrid one, the h_{base} is the magnetic field at the base grid patch that owns the $e_{cb,i}$, whereas $h_{s,j}$ denotes the jth subgrid patch with one edge falling onto the $e_{cb,i}$. Since L_c is different from L_f, the above is inaccurate in computing the curl of $\mathbf{H}$ to generate $e_{cb,i}$.

For better accuracy, we use an average length $L_{2D,ave}$ of the two patches along the direction perpendicular to the e_{cb} to evaluate the curl of $\mathbf{H}$, which is

$$L_{2D,ave} = \frac{L_c + L_f}{2}. \tag{41}$$

To utilize the average length, the row entry of $\mathbf{S}_h^{(i)}$ of the patches involving e_{cb} should be changed from the original $1/L_i$ (L_i being L_c or L_f) to $1/L_{2D,ave}$. We hence replace $1/L_i$ by $1/L_{2D,ave}$ for the rows corresponding to the e_{cb} unknowns, obtaining

$$\mathbf{S}_{total} = \mathbf{D}_1\left(\mathbf{S}_{cc} + \frac{L_f}{nL_c}\mathbf{P}^T\mathbf{S}_{ff}\mathbf{P}\right) \tag{42}$$

where

$$\mathbf{D}_1 = diag\{\{1\}_{\#e_{ci}}, \{1\}_{\#e_{fi}}, \{L_c/L_{2D,ave}\}_{\#e_{cb}}\}. \tag{43}$$

In this way, (40) becomes

$$\epsilon_i e_{cb,i} + \sigma_i e_{cb,i} = -\left[\frac{1}{L_{2D,ave}}\dot{h}_{base} - \frac{1}{nL_{2D,ave}}\sum_{j=1}^{n}\dot{h}_{s,j}\right] \tag{44}$$

which is accurate. However, since $\mathbf{S}_{ff}$ also involves e_{fi}, the constant coefficient $L_f/nL_c = 1/n^2$ in (42) scales the right-hand side corresponding to the e_{fi} as well, and hence the equation is changed. Again, we can scale the left-hand side of (39) in the same way to make the equation correct.

As a result, (39) becomes

$$\mathbf{D}_s\mathbf{D}_\epsilon\{\ddot{e}\} + \mathbf{D}_s\mathbf{D}_\sigma\{\dot{e}\} = -\mathbf{S}_{total}\{e\} \tag{45}$$

in which

$$\mathbf{D}_s = diag\{\{1\}_{\#e_{ci}}, \{1/n^2\}_{\#e_{fi}}, \{1\}_{\#e_{cb}}\} \tag{46}$$

and

$$\mathbf{S}_{total} = \mathbf{D}_1\mathbf{S}_t \tag{47}$$

where

$$\mathbf{S}_t = \mathbf{S}_{cc} + (1/n^2)\mathbf{P}^T\mathbf{S}_{ff}\mathbf{P}. \tag{48}$$

The stability of (45) is governed by the eigenvalues of $\mathbf{D}_\epsilon^{-1}\mathbf{D}_s^{-1}\mathbf{D}_1\mathbf{S}_t$. Since $\mathbf{D}_\epsilon^{-1}\mathbf{D}_s^{-1}\mathbf{D}_1$ is diagonal and symmetric positive definite, and $\mathbf{S}_t$ is SPD, the eigenvalues of $\mathbf{D}_\epsilon^{-1}\mathbf{D}_s^{-1}\mathbf{D}_1\mathbf{S}_t$ are nonnegative real. As a result, the resultant subgridding scheme is guaranteed to be stable. Meanwhile, the accuracy is also ensured via the choice of $\mathbf{P}$, and the use of average length across the base grid and the subgrid.

To realize a local time stepping, we transform (45) to the following system:

$$\begin{bmatrix} \mathbf{D}_\epsilon & 0 \\ 0 & \mathbf{D}_s\mathbf{D}_\epsilon \end{bmatrix}\begin{bmatrix} \ddot{e}_p \\ \ddot{e}_m \end{bmatrix} + \begin{bmatrix} \mathbf{D}_\sigma & 0 \\ 0 & \mathbf{D}_s\mathbf{D}_\sigma \end{bmatrix}\begin{bmatrix} \dot{e}_p \\ \dot{e}_m \end{bmatrix} + \begin{bmatrix} \mathbf{D}_1\mathbf{S}_{cc} & \mathbf{D}_1\mathbf{S}_{cc} \\ n^{-2}\mathbf{D}_1\mathbf{P}^T\mathbf{S}_{ff}\mathbf{P} & n^{-2}\mathbf{D}_1\mathbf{P}^T\mathbf{S}_{ff}\mathbf{P} \end{bmatrix}\begin{bmatrix} e_p \\ e_m \end{bmatrix} = b. \tag{49}$$

An explicit time marching is then performed on the e_p and e_m separately as follows:

$$\mathbf{D}_\epsilon\ddot{e}_p + \mathbf{D}_\sigma\dot{e}_p + \mathbf{D}_1\mathbf{S}_{cc}\{e\} = b_c \tag{50}$$

$$\mathbf{D}_1^{-1}\mathbf{D}_s\mathbf{D}_\epsilon\ddot{e}_m + \mathbf{D}_1^{-1}\mathbf{D}_s\mathbf{D}_\epsilon\dot{e}_m + n^{-2}\mathbf{P}^T\mathbf{S}_{ff}\mathbf{P}\{e\} = \mathbf{D}_1^{-1}b_f \tag{51}$$

$$\{e\} = e_p + e_m \tag{52}$$

which allows for a local time stepping without affecting stability.

B. Interpretation and Implementation in the Original FDTD Difference Equation-Based Framework

The formulas provided in this section above may appear abstract since matrix representations are used to derive the algorithm. However, if we do not use matrix operators, one cannot see a system-level picture clearly. Indeed, it is difficult to see how the change of one row of equation affects the stability of the whole numerical system, if one stays in the original framework of the FDTD composed of many differencing equations. In contrast, once the SPD operator is developed, we can readily explain it using the language of the original FDTD. Next, we provide an interpretation and show the implementation of the proposed algorithm in the original FDTD. We do so for both global time stepping, i.e., the same time step (restricted by the finest grid) is used in the base grid and the subgrid; and local time stepping, i.e., each grid is stably simulated using its own local time step.

1) Global Time Stepping: The procedure is as follows.

1) For e_{ci} unknowns, which are inside the base grid, they are solved in the same way as in the original FDTD. In other words, each e_{ci} at the current time step is obtained from the curl of $\mathbf{H}$ operation using the two $\mathbf{H}$ fields at previous time step located at the two patches that share the e_{ci}.
2) For magnetic field unknowns inside the base grid, they are also solved in the same way as in the original FDTD.
3) For e_{cb} unknowns, which reside on the interface between the subgrid and the base grid, we use the average of the H-fields at the n subgrid patches adjacent to the e_{cb}, and the H-field at the base grid patch having e_{cb}, to perform a curl of $\mathbf{H}$ operation. The length averaged from the base grid cell size and subgrid cell size is used for better accuracy.
4) The e_{fb} unknowns are obtained from $\mathbf{P}_{fc}e_{cb}$, which is nothing but to set them the same as the e_{cb} where the e_{fb} unknowns reside.
5) The e_{fi} and the magnetic field unknowns inside the subgrid are solved in the same way as that in the original FDTD.

As can be seen, only the e_{cb} and e_{fb} are different from the original FDTD in their generation. The time step of the above scheme is restricted by the smallest space step in the grid, which we term a global time step.

2) Local Time Stepping: For local time stepping, i.e., subgridding in time, all the unknowns, except for e_{cb}, are generated in the same way as above. For the e_{cb} unknown, we should do the following. At each time step of time marching, from the base grid, we know the H-field at previous time instant at the patch having e_{cb}, we use it to perform only a partial curl of $\mathbf{H}$ operation, which is $h_{base}/L_{2D,ave}$. In other words, we do not complete the curl of $\mathbf{H}$ operation using the H-fields from the subgrid. The partial curl of $\mathbf{H}$ evaluated from the base grid only provides one component of the e_{cb}, denoted by $e_{cb,p}$, but it allows all unknowns in the base grid to be generated using a large time step. For the subgrid, we use the time step restricted by the subgrid space step, and obtain the other half of the curl of $\mathbf{H}$ operation by taking the average of the n H-fields on the n subgrid patches adjacent to e_{cb}. Let such an average field be h_{sub}, we perform $-h_{sub}/L_{2D,ave}$ to obtain the other component of e_{cb} denoted by $e_{cb,m}$. Then adding the $e_{cb,p}$ and $e_{cb,m}$ makes the total e_{cb}. Since two different time steps are used, the addition is performed at the time instants of the smaller time step, where $e_{cb,p}$ is interpolated to provide a value at the desired time instants. Then the total e_{cb} is also known for the time instants of the larger time step. The time step ratio is the grid ratio, hence for one time step marching in the base grid, n steps of marching are performed in the subgrid.

V. SPD 3-D Subgridding Algorithm in Space and Time

A. 3-D Subgridding Operator

Different from 2-D cases, in addition to $\{e_{ci}\}$, $\{e_{cb}\}$, $\{e_{fi}\}$ unknowns, there are two sets of $\{e_{fb}\}$ unknowns. One set is located along the edges that overlap with $\{e_{cb}\}$, which we denote by $\{e_{fb,e}\}$; and the other set is on the faces of the interface between the base grid and the subgrid, which we denote by $\{e_{fb,f}\}$, as illustrated in Fig. 2. This set of $\{e_{fb,f}\}$ unknowns is unique for 3-D cases, which does not appear in 2-D scenarios. Since $\{e_{cb}\}$ is tangential to the subgrid interface, the 12 e_{cb} unknowns on a subgrid interface make a complete set to interpolate both $\{e_{fb,e}\}$ and $\{e_{fb,f}\}$ unknowns. Thus, we have

$$e_{fb} = \begin{bmatrix} e_{fb,f} \\ e_{fb,e} \end{bmatrix} = \mathbf{P}_{fc}e_{cb} \tag{53}$$

where

$$\mathbf{P}_{fc} = \begin{bmatrix} \mathbf{P}_{fc,f} \\ \mathbf{P}_{fc,e} \end{bmatrix} \tag{54}$$

with the upper part used to interpolate $\{e_{fb,f}\}$ and the lower part for interpolating $\{e_{fb,e}\}$. If a linear interpolation is used, for an arbitrary grid ratio n, the ith column of $\mathbf{P}_{fc}$ has the following nonzero entries located at the rows corresponding to the $\{e_{fb,f}\}$ and the $\{e_{fb,e}\}$ unknowns interpolated from the ith e_{cb}:

$$\mathbf{P}_{fc,i} = [\underbrace{\{(n-1)/n\}_n, \{(n-2)/n\}_n, \ldots, \{1/n\}_n}_{e_{fb,f} \text{ on face 1 of } e_{cb} \text{ and parallel to } e_{cb}}, \underbrace{\{(n-1)/n\}_n, \{(n-2)/n\}_n, \ldots, \{1/n\}_n}_{e_{fb,f} \text{ on face 2 of } e_{cb} \text{ and parallel to } e_{cb}}, \underbrace{\{1\}_n}_{e_{fb,e} \text{ that overlaps with } e_{cb}}]^T \tag{55}$$

in which the subscript of each set denotes the number of entries in the set. For example, the last set, $\{1\}_n$, is a set having n ones, each of which corresponds to one fine edge unknown $e_{fb,e}$ located along the e_{cb} edge. This set is, in fact, the $\mathbf{P}_{fc,e}$ in (54), which is the same as the $\mathbf{P}_{fc}$ in the 2-D scheme. The other two groups of entries of (55) make the part of $\mathbf{P}_{fc,f}$, yielding the $e_{fb,f}$ located on the two faces that share the e_{cb}. The first group from $\{(n-1)/n\}_n$ to $\{1/n\}_n$ corresponds to the $e_{fb,f}$ falling onto the first face and parallel to the e_{cb}, while the second group corresponds to the $e_{fb,f}$ falling onto the second face and parallel to the e_{cb}.

The $\mathbf{P}$ for 3-D problems is thus (21) but with the new 3-D $\mathbf{P}_{fc}$ shown in (55). Different from 2-D settings, $(\mathbf{P}^T\mathbf{P})^{-1}$ is not diagonal any more. In [15], we only use $\mathbf{P}_{fc,e}^T$ instead of a complete $\mathbf{P}_{fc}^T$ to develop a 3-D subgridding algorithm. Although the resulting $\mathbf{P}_{fc,e}^T\mathbf{P}_{fc,e}$ is diagonal, the information inside the subgrid cannot be utilized to solve the whole problem. In other words, the base grid solution is decoupled from the subgrid solution, which is inaccurate when strong inhomogeneity exists in the subgrid. Although the subgrid solution still depends on the base grid solution in the 3-D scheme of [15], the base grid solution is the same regardless of the content of the subgrid, which is its source of inaccuracy.

Based on the findings in 2-D cases, the $(\mathbf{P}^T\mathbf{P})^{-1}$ plays a role of averaging the contribution from the multiple subgrid patches to produce an accurate curl of $\mathbf{H}$ to generate e_{cb}. Therefore, it is feasible that we modify $(\mathbf{P}^T\mathbf{P})^{-1}$ to a diagonal matrix that makes the final system matrix SPD, and meanwhile let it perform an accurate operation of averaging. The details are as follows.

For each e_{cb} unknown, there is one column vector in $\mathbf{P}_{fc}$ to interpolate the e_{fb} unknowns. Consider the ith e_{cb}, thus, the ith row of $\mathbf{P}^T\mathbf{S}_{ff}\mathbf{P}$. It can be written as

$$\mathbf{P}_i^T\mathbf{S}_{ff}\mathbf{P} = \mathbf{P}_i^T\left[\mathbf{S}_{ff,g1}^{\mathrm{F1(i)}} + \mathbf{S}_{ff,g2}^{\mathrm{F1(i)}} + \mathbf{S}_{ff,g1}^{\mathrm{F2(i)}} + \mathbf{S}_{ff,g2}^{\mathrm{F2(i)}}\right]\mathbf{P} \tag{56}$$

where the superscripts $^{\mathrm{F1(i)}}$ and $^{\mathrm{F2(i)}}$ denote face 1 and face 2, respectively, which share the ith e_{cb}, as illustrated in Fig. 3. Using the patch-based formulation, the $\mathbf{S}_{ff}$ is nothing but the summation of the rank-1 matrix of each patch in the subgrid

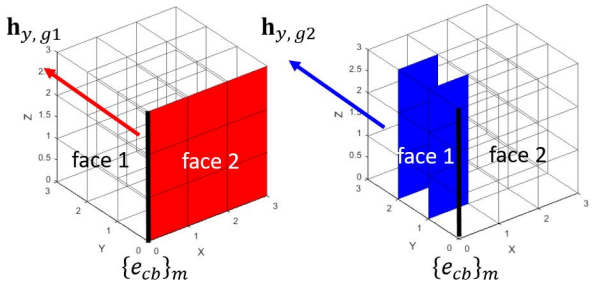

Fig. 3. Illustration of one e_{cb} (black), the two faces sharing e_{cb}, and the two groups of subgrid patches whose magnetic fields are used to generate e_{cb}.

region. Hence, when evaluating (56), we only need to identify which patch is selected by the row vector $\mathbf{P}_i^T$, i.e., involved in the multiplication with $\mathbf{P}_i^T$ and hence contributing to the product of $\mathbf{P}_i^T\mathbf{S}_{ff}$. Based on the expression of $\mathbf{P}_{fc,i}$ shown in (55), clearly, all patches that have an edge located on the two faces that share e_{cb}, and also parallel to the e_{cb}, will be selected. In addition, these patches can also be classified into two groups: one group falls onto face 1 and face 2, while the other group of patches are perpendicular to face 1, and face 2, respectively. In Fig. 3, the first group that falls onto face 2 (right face) of e_{cb} is shown and colored in red; while in the second group, the patches perpendicular to face 1 of e_{cb} are shown and colored in blue. The contribution from the first group of patches is denoted by $\mathbf{S}_{ff,g1}$, while the other is denoted by $\mathbf{S}_{ff,g2}$ in (56). For each of the two faces where the e_{cb} resides, both contributions exist.

The $\mathbf{S}_{ff,g1}$ term can be evaluated on each face as the following:

$$\begin{aligned}\mathbf{P}_i^T\mathbf{S}_{ff,g1}\mathbf{P}\{e\} = \mathbf{P}_i^T[&(\mathbf{S}_{h,11}\dot{h}_{11} + \cdots + \mathbf{S}_{h,n1}\dot{h}_{n1}) \\ &+ (\mathbf{S}_{h,12}\dot{h}_{12} + \cdots + \mathbf{S}_{h,n2}\dot{h}_{n2}) \\ &+ \cdots (\mathbf{S}_{h,1n}\dot{h}_{1n} + \cdots + \mathbf{S}_{h,nn}\dot{h}_{nn})]\end{aligned} \tag{57}$$

in which the $\mathbf{S}_h$ are from the first group of patches, which are those falling onto the face. For a grid ratio of n, it is evident that there are n^2 such patches, each of which is denoted by a row and a column index of the patch using subscripts. For example, h_{n1} denotes the magnetic field on the patch located in the first column (closest to the $e_{cb,i}$) and the nth row. Based on the expression of $\mathbf{P}_{fc,i}$, (57) can be readily evaluated and found as

$$\mathbf{P}_i^T\mathbf{S}_{ff,g1}\mathbf{P}\{e\} = \frac{\sum_{i=1}^n\sum_{j=1}^n \dot{h}_{ij}}{L_c}. \tag{58}$$

Clearly, the numerator represents the sum of all of the normal magnetic fields at the patches residing on the face. If we divide the above by n^2, then the numerator represents the average magnetic field located at the center of the face, i.e., the red point shown in Fig. 4. Thus, we have

$$\mathbf{P}_i^T\mathbf{S}_{ff,g1}\mathbf{P}\{e\} = n^2\frac{\dot{h}_{cnt}^{\mathrm{F}}}{L_c} \tag{59}$$

in which h_{cnt}^{F} stands for the magnetic field at the face center normal to the face and along the reference direction of the face.

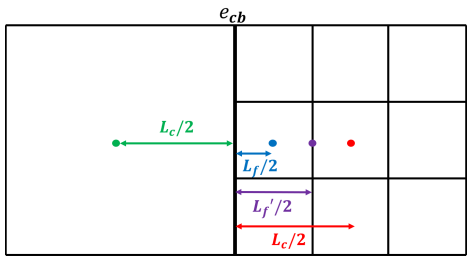

Fig. 4. Illustration of the magnetic field point corresponding to each term, and the average length for different patches.

Similarly, we can quantitatively evaluate the second group's contribution in (56), which is

$$\begin{aligned}\mathbf{P}_i^T\mathbf{S}_{ff,g2}\mathbf{P}\{e\} &= \mathbf{P}_i^T\big[\big(\mathbf{S}_{h,11}^{\perp}\dot{h}_{11}^{\perp}+\cdots+\mathbf{S}_{h,n1}^{\perp}\dot{h}_{n1}^{\perp}\big)\\ &\quad+\big(\mathbf{S}_{h,12}^{\perp}\dot{h}_{12}^{\perp}+\cdots+\mathbf{S}_{h,n2}^{\perp}\dot{h}_{n2}^{\perp}\big)\\ &\quad+\cdots\big(\mathbf{S}_{h,1,n-1}^{\perp}\dot{h}_{1,n-1}^{\perp}+\cdots+\mathbf{S}_{h,n,n-1}^{\perp}\dot{h}_{n,n-1}^{\perp}\big)\big]. \quad (60)\end{aligned}$$

Here the $\mathbf{S}_h^{\perp}$ is generated from patches that are perpendicular to the face, as those colored in blue in Fig. 3. There are $n-1$ columns of such patches on either of the two faces sharing the e_{cb}, and in each column there are n patches, and hence two subscripts are used for h in the above to denote the patch's, thus h's location. Again, based on the expressions of $\mathbf{P}_{fc,i}$ and $\mathbf{S}_h$, we find the above to be

$$\begin{aligned}\mathbf{P}_i^T\mathbf{S}_{ff,g2}\mathbf{P}\{e\} &= \frac{n-1}{nL_f}\sum_{i=1}^{n}\dot{h}_{i1}^{\perp}+\frac{n-2}{nL_f}\sum_{i=1}^{n}\dot{h}_{i2}^{\perp}\\ &\quad+\cdots+\frac{1}{nL_f}\sum_{i=1}^{n}\dot{h}_{i,n-1}^{\perp}. \quad (61)\end{aligned}$$

If we divide the above by $n(n-1)/2$, then the summation can be viewed as an average magnetic field in the direction perpendicular to the patches, thus parallel to the face where the patches are attached. Since the patches involved in (61) are immediately adjacent to the face, the resulting magnetic field after averaging can be viewed as a field located at the point whose distance to the e_{cb} is $L_f/2$, as shown by the blue point in Fig. 4, and on the face parallel to the patch. Let this field be h_{sub}. We have

$$\mathbf{P}_i^T\mathbf{S}_{ff,g2}\mathbf{P}\{e\} = \tfrac{n(n-1)}{2L_f}\dot{h}_{sub}. \quad (62)$$

Take face 2, occupied by all red patches shown in Fig. 3, as an example. On this face, the first group of patches' contribution, as shown in (59), after averaging, produces a magnetic field located at the center of the face and normal to the face. This point is the red point shown in Fig. 4. The magnetic field along the same direction is also produced by the second group of patches on face 1, i.e., $\mathbf{P}_i^T\mathbf{S}_{ff,g2}^{\mathrm{F1(i)}}\mathbf{P}\{e\}$. As shown in (62), this component, after averaging, can be viewed as the magnetic field located at the point whose distance to the e_{cb} is $L_f/2$, thus the blue point in Fig. 4. We hence can use these two magnetic fields to do an average to obtain the magnetic field located at the midpoint of the two fields, whose distance to the e_{cb} is $L_f{}' = (L_f + L_c)/2$. This magnetic field together with the magnetic field at the center of the adjacent base grid patch, marked as a green point in Fig. 4, can then be used to generate an accurate curl of $\mathbf{H}$ to produce e_{cb}. Similar to the treatment in 2-D, we need to use the average length of L_c and $L_f{}'$ to achieve a better accuracy in computing the curl of $\mathbf{H}$. Thus, the average length, L_{ave}, is

$$L_{ave} = \frac{L_c + L_f{}'}{2} = \frac{3L_c + L_f}{4}. \quad (63)$$

Based on the aforementioned, we compute e_{cb} in the following way:

$$\begin{aligned}&\epsilon_i\ddot{e}_{cb,i}+\sigma_i\dot{e}_{cb,i}\\ &\quad=-\big[\alpha\mathbf{P}_i^T\mathbf{S}_{cc}\mathbf{P}+\beta\mathbf{P}_i^T\mathbf{S}_{ff,g1}\mathbf{P}+\gamma\,\mathbf{P}_i^T\mathbf{S}_{ff,g2}\mathbf{P}\big]\{e\} \quad (64)\end{aligned}$$

where

$$\alpha = \frac{L_c}{L_{ave}} \quad (65)$$

$$\beta = \frac{L_c}{2n^2L_{ave}} \quad (66)$$

and

$$\gamma = \frac{L_f}{n(n-1)L_{ave}}. \quad (67)$$

Substituting (59) and (62) into (64), it can be seen that (64) is nothing but to compute

$$\begin{aligned}\epsilon_i\ddot{e}_{cb,i}+\sigma_i\dot{e}_{cb,i} &= \frac{\dot{h}_{base}^{\mathrm{F1(i)}}-0.5\big(\dot{h}_{cnt}^{\mathrm{F1(i)}}+\dot{h}_{sub}^{\mathrm{F1(i)}}\big)}{L_{ave}}\\ &\quad+\frac{\dot{h}_{base}^{\mathrm{F2(i)}}-0.5\big(\dot{h}_{cnt}^{\mathrm{F2(i)}}+\dot{h}_{sub}^{\mathrm{F2(i)}}\big)}{L_{ave}} \quad (68)\end{aligned}$$

where the h_{base} is the magnetic field at the center of the base grid patch that has e_{cb}, and its superscript denotes the subgrid face that is on the same plane as the base grid patch. Hence, (64) produces an accurate curl of $\mathbf{H}$ for generating e_{cb}.

Based on (64), now we can write the whole system of equations for solving all unknowns as

$$\mathbf{D}_s\mathbf{D}_\epsilon\{\ddot{e}\}+\mathbf{D}_s\mathbf{D}_\epsilon\{\dot{e}\} = -\mathbf{S}_{total}\{e\} \quad (69)$$

in which

$$\mathbf{D}_s = diag\{\{1\}_{\#e_{ci}},\{\gamma/\alpha\}_{\#e_{fi}},\{1\}_{\#e_{cb}}\} \quad (70)$$

and

$$\begin{aligned}\mathbf{S}_{total} = \mathbf{D}_1\Big(&\mathbf{S}_{h,c}\mathbf{D}_{\mu_c^{-1}}\mathbf{S}_{e,c}+\frac{\beta}{\alpha}\mathbf{P}^T\mathbf{S}_{ff,g1}\mathbf{P}\\ &+\frac{\gamma}{\alpha}\mathbf{P}^T(\mathbf{S}_{ff,g2}+\mathbf{S}_{ff,g3})\mathbf{P}\Big) \quad (71)\end{aligned}$$

with

$$\mathbf{D}_1 = diag\{\{1\}_{\#e_{ci}},\{1\}_{\#e_{fi}},\{\alpha\}_{\#e_{cb}}\}. \quad (72)$$

In (71), the subscript $g3$ denotes the third group of patches, which are inside the subgrid. The $\mathbf{D}_s$ is used in (69), because when $\mathbf{S}_{ff,g2}$ term is scaled by γ/α, the field internal to the subgrid, i.e., e_{fi}, is also scaled by this coefficient. Hence, by left scaling the entire system by $\mathbf{D}_s$, we keep the solution of e_{fi} the same as before. It is obvious that the matrix in the big parenthesis of (71) is SPD, and hence the final numerical system remains to have nonnegative real eigenvalues. Meanwhile, we have taken the accuracy into account in generating the e_{cb} unknowns.

B. Interpretation and Implementation in the Original FDTD Difference Equation-Based Framework

The proposed 3-D subgridding operator can be interpreted, and implemented in the original FDTD as follows.

1) Global Time Stepping: The procedure is as follows.

1) For e_{ci} and magnetic field unknowns, which are inside the base grid, they are solved in the same way as in the original FDTD.
2) For an e_{cb} unknown, we obtain the H-fields at the n^2 subgrid patches on one face (for example, face 1) having the e_{cb}, and then take its average. Let this be h_{cnt}. We then obtain the weighted sum of the magnetic fields shown in the right-hand side of (61) on the other face (face 2) that has e_{cb}. Dividing the sum by $n(n-1)/2$, we obtain h_{sub}. Using the H-field at the base grid patch that has the e_{cb} on the same plane as face 1, denoted by h_{base}, we can perform a curl of $\mathbf{H}$ operation as shown in (68) to obtain e_{cb}, together with the h_{cnt} generated on face 2, the h_{sub} from face 1, and the h_{base} on the other base grid patch.
3) The e_{fb} unknowns are obtained from $\mathbf{P}_{fc}e_{cb}$.
4) The e_{fi} and the magnetic field unknowns inside the subgrid are solved in the same way as that in the original FDTD.

Similar to 2-D, only the e_{cb} and e_{fb} are generated differently.

2) Local Time Stepping: For local time stepping, i.e., subgridding in time, all the unknowns, except for e_{cb}, is generated in the same way as above. For the e_{cb} unknown, we do the following. At each time step of time marching, from the base grid, we know the H-field at previous time step at the two patches having e_{cb}, we use it to perform only a partial curl of $\mathbf{H}$ operation, which is $(h^1_{base}+h^2_{base})/L_{ave}$. In other words, we do not complete the curl of $\mathbf{H}$ operation using the H-fields from the subgrid. The partial curl of $\mathbf{H}$ evaluated from the base grid only provides one component of the e_{cb}, denoted by $e_{cb,p}$, but it allows all unknowns in the base grid to be generated using a large time step. For the subgrid, we use the time step restricted by the subgrid space step and obtain the other half of the curl of $\mathbf{H}$ operation by evaluating the H-fields in every subgrid patch and then obtaining h_{sub} and h_{cnt} on both faces inside the subgrid that has e_{cb}, using which we obtain the other component of e_{cb}, $e_{cb,m}$, which correspond to the right-hand side of (68) with the two base-grid fields excluded. Then adding the $e_{cb,p}$ and $e_{cb,m}$ makes the total e_{cb}.

VI. Numerical Results

In this section, we simulate a variety of 2- and 3-D examples with uniform or highly inhomogeneous materials to examine the performance of the proposed subgridding algorithms in stability, accuracy, and efficiency.

A. 2-D Free-Space Wave Propagation

We first simulate a free-space wave propagation problem in a 2-D region of size 0.5 m × 0.5 m. The base grid size is $L_c = 0.1$ m, and the subgrid is located at the center of the base grid. The grid ratio n ranges from 2, 5, 20, to 100.

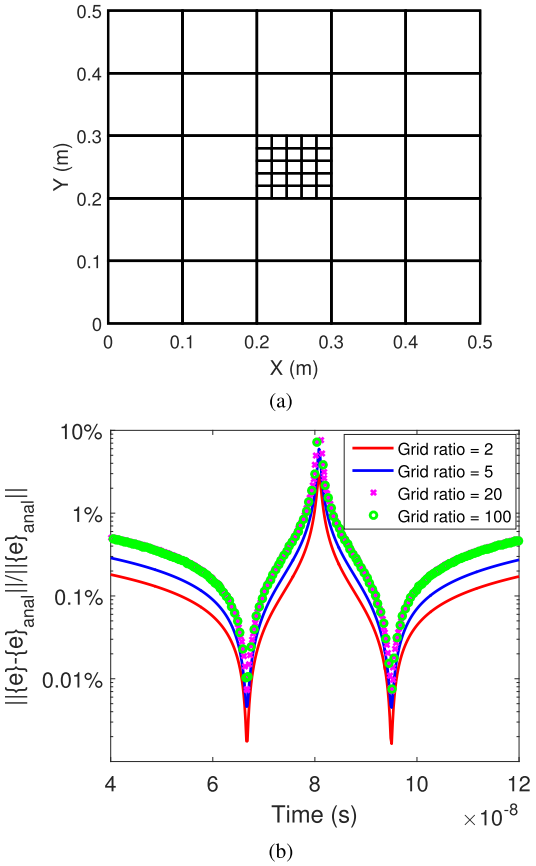

Fig. 5. Simulation of a 2-D wave propagation problem. (a) Grid (for the case of $n = 5$). (b) Entire solution error versus time for different grid ratios ($n = 2, 5, 20, 100$) generated using the local time stepping.

In Fig. 5(a), the grid for a grid ratio of $n = 5$ is shown. The time step used in the base grid is $dt_c = 1.9 \times 10^{-10}$ s, which is determined by L_c, and the time step for the subgrid region allowed by the stability condition is $dt_f = dt_c/n$. The $\mathbf{E}^{inc}$ is $\hat{y}2(t - t_0 - x/c)e^{(t-t_0-x/c)^2/\tau^2}$ with $c = 3 \times 10^8$ m/s, $\tau = 2\times 10^{-8}$ s, and $t_0 = 4\tau$. All the boundaries are terminated by exact absorbing boundary conditions, i.e., known fields for the given problem. The entire solution error at each time step as compared to the analytical solution is assessed by

$$\text{Entire Solution Error} = \frac{\|\{e\} - \{e\}_{anal}\|}{\|\{e\}_{anal}\|} \tag{73}$$

where $\|\cdot\|$ denotes the norm of the vector, and 2-norm is used. In addition, the vector $\{e\}$ is of length N_e, i.e., including all electric field unknowns in the computational domain. In Fig. 5(b), we plot (73) for different grid ratios, where $\{e\}$ denotes the vector of all electric field unknowns in the grid. It is clear to see that the simulated fields agree with the analytical solution very well. The center peak error is due to a comparison with zero. We also simulate the same problem using the conventional FDTD method and compare the CPU run time of the two methods in Table I for different grid ratios. It is obvious that the proposed method is more efficient since the number of unknowns to solve is greatly reduced, and the time step used in the base grid is also significantly enlarged.

TABLE I

CPU TIME COMPARISON OF AN EXAMPLE FOR DIFFERENT GRID RATIOS USING LOCAL TIME STEPPING

Grid ratio	2	5	20	100
Time (s) of FDTD	0.0487	0.5458	37.8527	5522.14
Time (s) of this method	0.0324	0.0555	0.4359	38.47
Speedup	1.50	9.83	86.84	143.54

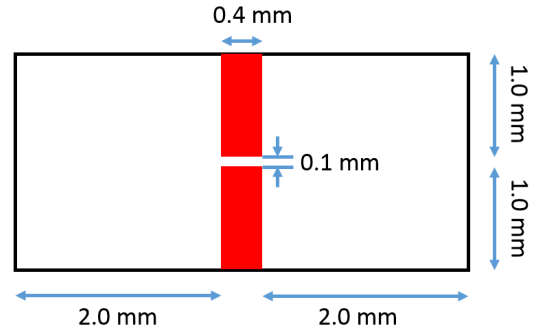

(a)

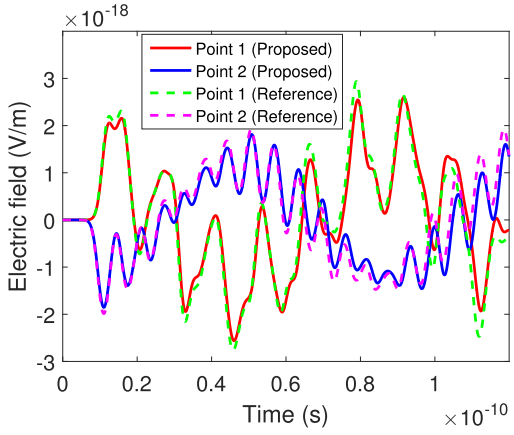

(b)

Fig. 6. Simulation of a PEC cavity with conducting fins separated by a thin gap. (a) Structure. (b) Simulated electric fields using local time stepping.

B. 2-D PEC Cavity With Conducting Fins

Next, a PEC cavity with two conducting fins separated by a thin gap, as illustrated in Fig. 6(a), is simulated. The conductivity of the fins is 5.8×10^7 S/m. A current source is launched at the middle of the fin gap vertically, and with a Gaussian derivative pulse of $-\tau^2 \exp(-(t-t_0)^2/\tau^2)$, with $\tau = 2\times 10^{-12}$ s, and $t_0 = 4\tau$. The coarse grid size is $L_c = 0.1$ mm, and the subgrid region, having a grid ratio of $L_c/L_f = 4$, is located between the two fins. The time step used in the subgrid is $dt_f = 4.2 \times 10^{-14}$ s, which is determined by L_f. The fields simulated from this method at two points, (1, 1.05) and (2.85, 1.5) mm, are plotted in Fig. 6(b) and compared with the conventional FDTD results. Very good agreement is observed. The conventional FDTD method, using a uniform grid, takes 6.68 s to finish the simulation while the proposed subgridding method only takes 0.84 s.

C. 3-D Free-Space Wave Propagation

The third example is a free-space wave propagation problem in a 3-D box. The size of the computational domain in each direction is 0.5 m. Along all directions, the coarse space step is $L_c = 0.1$ m. The subgrid is located at the center having a grid ratio n ranging from 2, 4, 10, to 20, making the fine space step $L_f = L_c/n$. The $\mathbf{E}^{inc}$ is $\hat{y}2(t - t_0 - x/c)e^{(t-t_0-x/c)^2/\tau^2}$ with $c = 3 \times 10^8$ m/s, $\tau = 2 \times 10^{-8}$ s, and $t_0 = 4\tau$. Again, all of the boundaries are terminated by exact absorbing boundary conditions. In Fig. 7, we first plot the simulated electric fields at two observation points in comparison with the analytical solution for grid ratio $n = 4$. Point 1 is at $(0.1, 0.05, 0.1)$ m and it is inside the base grid, while Point 2 is at $(0.225, 0.225, 0.2125)$ m, which is inside the subgrid. As can be seen, the electric fields solved from the proposed method have an excellent agreement with analytical results. We also plot the entire solution error at each time step as compared to the analytical solution, $\|\{e\} - \{e\}_{anal}\|/\|\{e\}_{anal}\|$, versus time in Fig. 8 for different grid ratios. As can be observed, the proposed method is not only accurate at selected observation points but also accurate at all other points. The center peak error is again due to a comparison with zero. In Fig. 9, we compare the accuracy of the proposed local time stepping with that of the global one. A grid ratio of 4 is considered. Instead of using the smallest time step dt_f everywhere, we use dt_c in the base grid, which is chosen to be 2, 3, and up to n times as large as the dt_f. As can be seen from Fig. 9, the stability is maintained, and the accuracy is not sacrificed.

In addition, in this example, we compare the difference between the proposed SPD operator shown in (69) which has

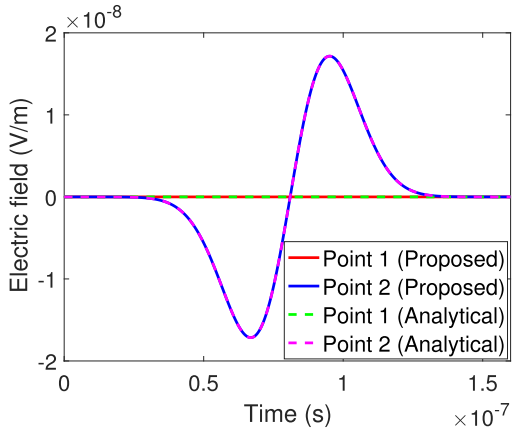

Fig. 7. Simulated electric fields at two observation points in comparison with reference analytical solutions of a 3-D wave propagation problem.

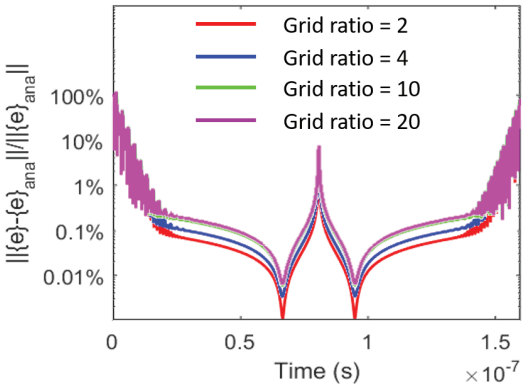

Fig. 8. Entire solution error versus time for different grid ratios of a 3-D wave propagation problem using the global time stepping.

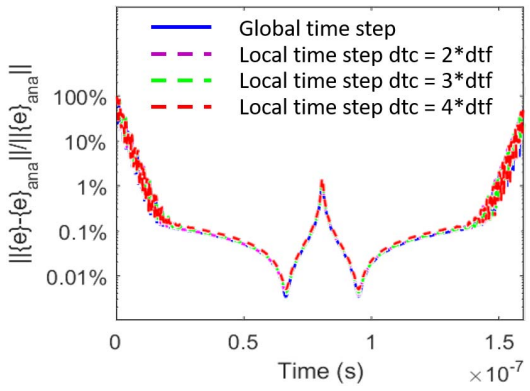

Fig. 9. Entire solution error versus time of a 3-D wave propagation problem, using local time stepping, with different time steps in the base grid.

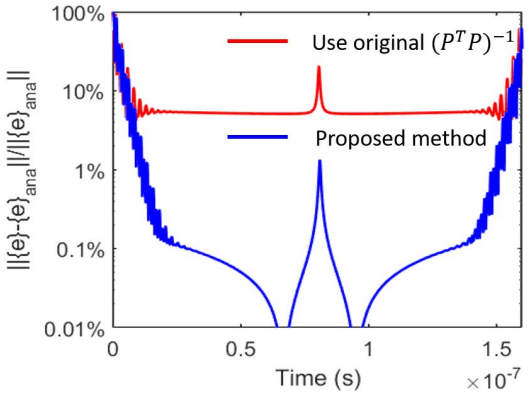

Fig. 10. Accuracy comparison between using (69) and using (33) of a 3-D wave propagation problem.

accuracy taken into account, and the preliminary one shown in (33), where $(\mathbf{P}^T\mathbf{P})^{-1}$ is kept as it is without modifications. We find complex eigenvalues such as $3.9384e19 \pm 1.6543e4i$ from (33), thus the stability cannot be guaranteed although in this case the imaginary part is small. Meanwhile, the accuracy is not as good as (69), where $(\mathbf{P}^T\mathbf{P})^{-1}$ is modified to perform an accurate averaging for mismatched grid sizes. The accuracy comparison can be seen from Fig. 10.

We also simulate this 3-D wave propagation problem to a very late time when the number of time steps is more than 1 000 000, the result of which is shown in Fig. 11. As can be seen, after the early time response, the fields are stably simulated as zero in the late time.

D. 3-D PEC Cavity With an Inhomogeneous Subgrid Region

Next we simulate a 3-D cavity excited by a current source, which has an inhomogeneous subgrid region, to examine the accuracy of the proposed algorithms in such a setting. The cavity is 1 cm long in all directions and terminated by a PEC boundary condition. The base grid size along each direction is 1 mm, except for the small cube centered at $(4.5, 4.5, 4.5)$ mm, which is illustrated in Fig. 12. This center cube is 1 mm long in all directions and filled with inhomogeneous materials, while the base grid has a dielectric constant of 3. The center cube is further subdivided with a grid size of 0.2 mm, resulting in 125 fine cells. To examine the capability of the proposed work in handling inhomogeneity, each subgrid cell's dielectric constant is set as a random number in the range of 1–125.

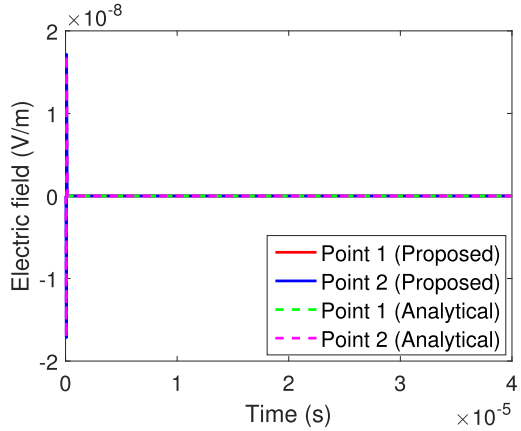

Fig. 11. Late-time simulation result from the proposed method versus analytical result of a 3-D wave propagation problem.

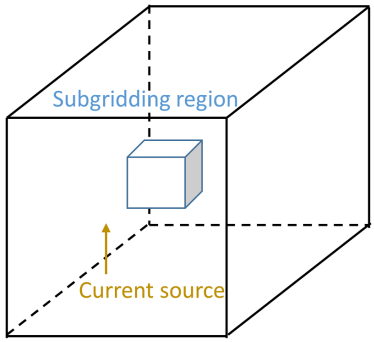

Fig. 12. Structure details of a 3-D cavity excited by a current source.

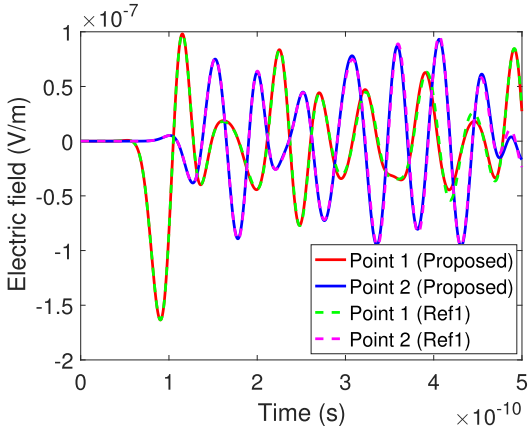

Fig. 13. Electric fields at two observation points using the proposed method versus reference results of a 3-D cavity example.

A current probe is placed at $(3, 3, 3.5)$ mm. The current has a Gaussian pulse whose waveform is $\hat{z}\tau e^{-(t-t_0)^2/\tau^2}$ with $\tau = 2.0 \times 10^{-11}$ s and $t_0 = 4\tau$. As a reference, we also simulate the same problem using the method in [14], which is an unsymmetrical subgridding method but can handle such inhomogeneous problems accurately. The time step allowed by the method in [14] is $dt = 3.8 \times 10^{-13}$ s. In Fig. 13, the electric fields sampled at Point 1 $(2, 2, 1.5)$ mm and Point 2 $(8, 8, 7.5)$ mm are plotted in comparison with the reference solution generated using the method of [14] (labeled as Ref1 in Fig. 13). It can be seen that the accuracy of the proposed method is very good. This shows the proposed new SPD method is able to handle inhomogeneous problems

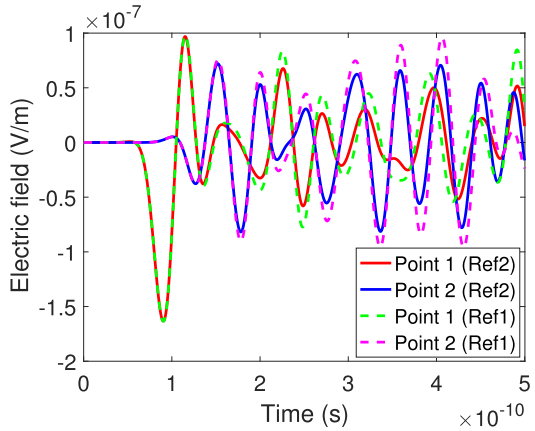

Fig. 14. Electric fields at two observation points using method in [15] versus reference results of a 3-D cavity example.

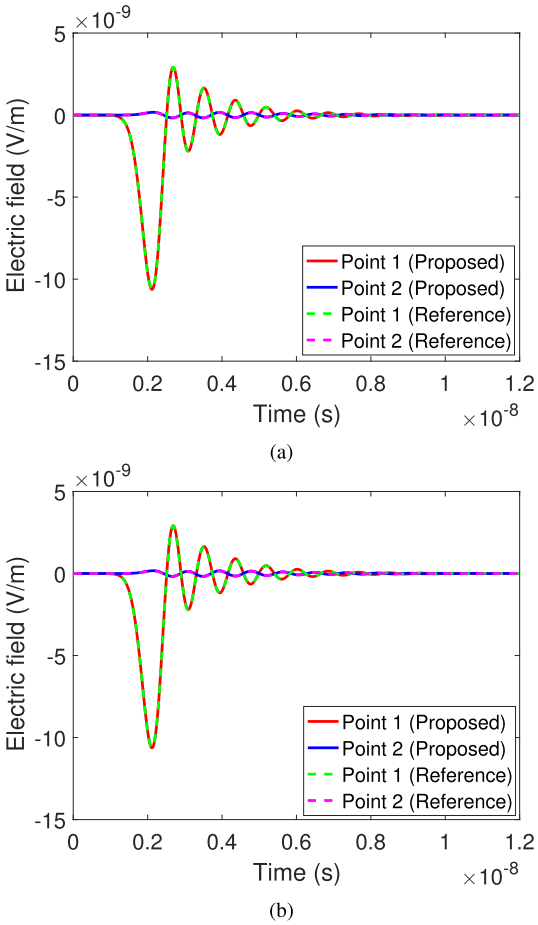

Fig. 15. Simulated electric fields at two observation points in comparison with reference results of a 3-D inhomogeneous phantom head example. (a) Global time stepping is used. (b) Local time stepping is used.

accurately. For comparison, the symmetric semi-definite method in [15] is used to simulate the same problem. As can be seen from Fig. 14, the results of [15] (labeled as Ref2) are not as accurate as the proposed method when compared to the reference solution. This is due to the fact that the electric fields shared by the base grid and the subgrid are solved from the base grid only in [15] to build an SPD system. This scheme cannot capture the variation in fields resulting from the inhomogeneous subgrid region.

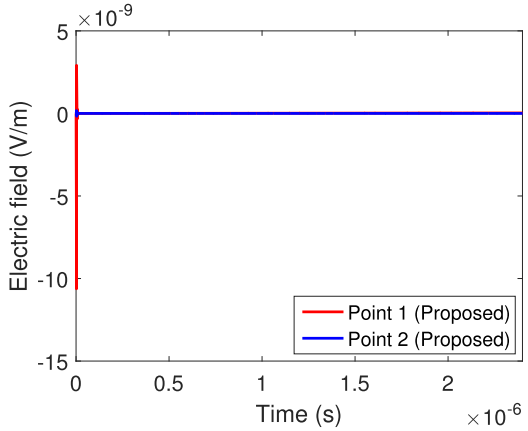

Fig. 16. Electric fields simulated over one million time steps of a 3-D inhomogeneous phantom head example.

E. Inhomogeneous 3-D Phantom Head Beside a Wire Antenna

In this example, we simulate a large-scale phantom head beside a wire antenna, which involves many inhomogeneous materials [14]. The size of the phantom head is 28.16 × 28.16 × 17.92 cm. All the boundaries are truncated by perfect magnetic conducting conditions. The wire antenna is located at (3.52, 3.52, 2.52) cm, with a current pulse of $\hat{z}2(t-t_0)e^{-(t-t_0)^2/\tau^2}$ with $\tau = 5.0 \times 10^{-10}$ s and $t_0 = 4\tau$. The base grid size along x-, y-, and z-directions is 4.4, 4.4, and 5.6 mm, respectively. To capture fine tissues, the base grid cell centered at (14.3, 14.3, 9.24) cm is subdivided into subgrid cells in all directions with a grid ratio of 4, making the subgrid grid size along x-, y-, and z-directions as 1.1, 1.1, and 1.4 mm, respectively. Again, we use the unsymmetrical subgridding method [14] as our reference. Due to the existence of the subgrid, the unsymmetrical subgridding method [14] must use a time step of 2.2×10^{-12} s across the whole grid to ensure stability. In contrast, the proposed new method allows for a larger time step $dt_c = 8.8 \times 10^{-12}$ s in the base grid. In Fig. 15(a), the electric fields at two observation points whose locations are (3.52, 3.52, 15.96) and (24.64, 3.52, 15.96) cm are plotted in comparison with the reference results obtained using a global time step. In Fig. 15(b), the electric fields obtained from a local time stepping at the same observation points are plotted. It is clear that the two sets of results agree well. The unsymmetrical subgridding method [14] uses 549 s to finish the simulation. In contrast, the proposed subgridding method only costs 345 s using a global time step, and 209 s when using a local time step.

The original number of time steps simulated is 5455 with the proposed method. We also simulate this example to a very late time when the number of time steps is more than 1 091 000. As shown in Fig. 16, no late time instability is observed.

VII. Conclusion

In this article, an SPD FDTD subgridding method in both space and time is developed for fast FDTD simulations. First, we provide an algebraic method to systematically derive an SPD subgridding operator for the FDTD in both space and time. This method yields a framework for developing a series

of SPD subgridding operators. We then take the accuracy into account and develop 2- and 3-D subgridding algorithms which are not only SPD for arbitrary grid ratios but also accurate for analyzing general inhomogeneous problems. The stability is guaranteed by construction, because the eigenvalues of the resulting SPD system matrix are nonnegative real. Furthermore, the time step of each grid for stability is determined by the time step local to the grid. Thus, the base grid time step is not restricted by the subgrid region, further accelerating the simulation. We also provide an interpretation of the proposed algorithms in the original FDTD framework and show how to implement them easily. Numerous numerical experiments have been carried out. Comparisons with both analytical solutions and state-of-the-art subgridding algorithms have demonstrated the accuracy, efficiency, and stability of the proposed new subgridding algorithms.

REFERENCES

[1] K. Yee, "Numerical solution of initial boundary value problems involving Maxwell's equations in isotropic media," *IEEE Trans. Antennas Propag.*, vol. AP-14, no. 3, pp. 302–307, May 1966.

[2] A. Taflove and S. C. Hagness, *Computational Electrodynamics: The Finite-Difference Time-Domain Method*. Boston, MA, USA: Artech House, 2000.

[3] S. Zivanovic, K. Yee, and K. Mei, "A subgridding method for the time-domain finite-difference method to solve Maxwell's equations," *IEEE Trans. Microw. Theory Techn.*, vol. 39, no. 3, pp. 471–479, Mar. 1991.

[4] D. Prescott and N. Shuley, "A method for incorporating different sized cells into the finite-difference time-domain analysis technique," *IEEE Microw. Guided Wave Lett.*, vol. 2, no. 11, pp. 434–436, Nov. 1992.

[5] M. White, M. Iskander, and Z. Huang, "Development of a multigrid FDTD code for three-dimensional applications," *IEEE Trans. Antennas Propag.*, vol. 45, no. 10, pp. 1512–1517, Oct. 1997.

[6] M. Chevalier, R. Luebbers, and V. Cable, "FDTD local grid with material traverse," *IEEE Trans. Antennas Propag.*, vol. 45, no. 3, pp. 411–421, Mar. 1997.

[7] M. White, Z. Yun, and M. Iskander, "A new 3D FDTD multigrid technique with dielectric traverse capabilities," *IEEE Trans. Microw. Theory Techn.*, vol. 49, no. 3, pp. 422–430, Mar. 2001.

[8] M. Okoniewski, E. Okoniewska, and M. Stuchly, "Three-dimensional subgridding algorithm for FDTD," *IEEE Trans. Antennas Propag.*, vol. 45, no. 3, pp. 422–429, Mar. 1997.

[9] P. Thoma and T. Weiland, "A consistent subgridding scheme for the finite difference time domain method," *Int. J. Numer. Model.*, vol. 9, no. 5, pp. 359–374, Sep. 1996.

[10] O. Podebrad, M. Clemens, and T. Weiland, "New flexible subgridding scheme for the finite integration technique," *IEEE Trans. Magn.*, vol. 39, no. 3, pp. 1662–1665, May 2003.

[11] L. Kulas and M. Mrozowski, "Reciprocity principle for stable subgridding in the finite difference time domain method," in *Proc. EUROCON-Int. Conf. Comput. Tool*, Sep. 2007.

[12] K. Xiao, D. J. Pommerenke, and J. L. Drewniak, "A three-dimensional FDTD subgridding algorithm with separated temporal and spatial interfaces and related stability analysis," *IEEE Trans. Antennas Propag.*, vol. 55, no. 7, pp. 1981–1990, Jul. 2007.

[13] J. Yan and D. Jiao, "Accurate and stable matrix-free time-domain method in 3-D unstructured meshes for general electromagnetic analysis," *IEEE Trans. Microw. Theory Techn.*, vol. 63, no. 12, pp. 4201–4214, Dec. 2015.

[14] J. Yan and D. Jiao, "An unsymmetric FDTD subgridding algorithm with unconditional stability," *IEEE Trans. Antennas Propag.*, vol. 66, no. 8, pp. 4137–4150, Aug. 2018.

[15] J. Yan and D. Jiao, "Symmetric positive semidefinite FDTD subgridding algorithms for arbitrary grid ratios without compromising accuracy," *IEEE Trans. Microw. Theory Techn.*, vol. 65, no. 12, pp. 5084–5095, Dec. 2017.

[16] M. Gaffar and D. Jiao, "An explicit and unconditionally stable FDTD method for electromagnetic analysis," *IEEE Trans. Microw. Theory Techn.*, vol. 62, no. 11, pp. 2538–2550, Nov. 2014.

[17] J. Yan and D. Jiao, "Fast explicit and unconditionally stable FDTD method for electromagnetic analysis," *IEEE Trans. Microw. Theory Techn.*, vol. 65, no. 8, pp. 2698–2710, Aug. 2017.

[18] K. Zeng and D. Jiao, "Symmetric positive semi-definite FDTD subgridding algorithm in both space and time," in *Proc. IEEE Int. Symp. AP*, Jul. 2018.

Kaiyuan Zeng (Student Member, IEEE) received the B.S. degree in electronic engineering and information science from the University of Science and Technology of China, Hefei, China, in 2012, and the Ph.D. degree in electrical engineering from Purdue University, West Lafayette, IN, USA, in May 2019.

He has been an Analog Engineer with the Assembly and Test Technology Development (ATTD) Division, Intel Corporation, Chandler, AZ, USA, since June 2019. His current research interests include signal and power integrity analysis, RF design, computational electromagnetics, and circuit and component design.

Dr. Zeng was a recipient of the Honorable Mention Award of the IEEE International Symposium on Antennas and Propagation in 2018 and the Best Student Paper Award from the IEEE Wireless and Microwave Technology Conference in 2015.

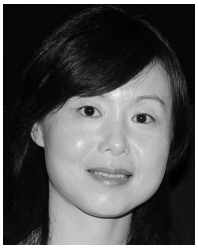

Dan Jiao (Fellow, IEEE) received the Ph.D. degree in electrical engineering from the University of Illinois at Urbana–Champaign, Champaign, IL, USA, in 2001.

She then worked at the Technology Computer-Aided Design (CAD) Division, Intel Corporation, Santa Clara, CA, USA, until September 2005, as a Senior CAD Engineer, a Staff Engineer, and a Senior Staff Engineer. In September 2005, she joined Purdue University, West Lafayette, IN, USA, as an Assistant Professor with the School of Electrical and Computer Engineering, where she is currently a Professor. She has authored 3 book chapters and over 300 articles in refereed journals and international conferences. Her current research interests include computational electromagnetics, high-frequency digital, analog, mixed-signal, and RF integrated circuit (IC) design and analysis, high-performance VLSI CAD, modeling of microscale and nanoscale circuits, applied electromagnetics, fast and high-capacity numerical methods, fast time-domain analysis, scattering and antenna analysis, RF, microwave, and millimeter-wave circuits, wireless communication, and bioelectromagnetics.

Dr. Jiao received the 2013 S. A. Schelkunoff Prize Paper Award of the IEEE Antennas and Propagation Society, which recognizes the Best Article published in the IEEE TRANSACTIONS ON ANTENNAS AND PROPAGATION during the previous year. She was also a recipient of the 2010 Ruth and Joel Spira Outstanding Teaching Award, the 2008 National Science Foundation (NSF) CAREER Award, the 2006 Jack and Cathie Kozik Faculty Start Up Award (which recognizes an Outstanding New Faculty Member of the School of Electrical and Computer Engineering, Purdue University), a 2006 Office of Naval Research (ONR) Award under the Young Investigator Program, the 2004 Best Paper Award presented at the Intel Corporation's annual corporate-wide technology conference (Design and Test Technology Conference) for her work on generic broadband model of high-speed circuits, the 2003 Intel Corporation's Logic Technology Development (LTD) Divisional Achievement Award, the Intel Corporation's Technology CAD Divisional Achievement Award, the 2002 Intel Corporation's Components Research the Intel Hero Award (Intel-wide she was the tenth recipient), the Intel Corporation's LTD Team Quality Award, and the 2000 Raj Mittra Outstanding Research Award presented by the University of Illinois at Urbana–Champaign. She was among the 21 women faculty selected across the country as the 2014–2015 fellow of Executive Leadership in Academic Technology and Engineering (ELATE) at Drexel, a national leadership program for women in the academic STEM fields. She has been named a University Faculty Scholar by Purdue University since 2013. She was among the 85 engineers selected throughout the nation for the National Academy of Engineering's 2011 U.S. Frontiers of Engineering Symposium. She has served as a reviewer for many IEEE journals and conferences. She is an Associate Editor of the IEEE TRANSACTIONS ON COMPONENTS, PACKAGING, AND MANUFACTURING TECHNOLOGY and an Associate Editor of the IEEE JOURNAL ON MULTISCALE AND MULTIPHYSICS COMPUTATIONAL TECHNIQUES.